Analysis of the Biological and Chemical Reactivity of Zeolite-Based Aluminosilicate Fibers and Particulates

Estelle Fach,[1] W. James Waldman,[2,3] Marshall Williams,[3] John Long,[4] Richard K. Meister,[4] and Prabir K. Dutta[1]

[1]Department of Chemistry, [2]Department of Pathology, [3]Department of Molecular Virology, Immunology, and Medical Genetics, and [4]Department of Veterinary Biosciences, The Ohio State University, Columbus, Ohio, USA

Environmental and/or occupational exposure to minerals, metals, and fibers can cause lung diseases that may develop years after exposure to the agents. The presence of toxic fibers such as asbestos in the environment plus the continuing development of new mineral or vitreous fibers requires a better understanding of the specific physical and chemical features of fibers/particles responsible for bioactivity. Toward that goal, we have tested aluminosilicate zeolites to establish biological and chemical structure–function correlations. Zeolites have known crystal structure, are subject to experimental manipulation, and can be synthesized and controlled to produce particles of selected size and shape. Naturally occurring zeolites include forms whose biological activity is reported to range from highly pathogenic (erionite) to essentially benign (mordenite). Thus, we used naturally occurring erionite and mordenite as well as an extensively studied synthetic zeolite based on faujasite (zeolite Y). Bioactivity was evaluated using lung macrophages of rat origin (cell line NR8383). Our objective was to quantitatively determine the biological response upon interaction of the test particulates/fibers with lung macrophages and to evaluate the efficacy of surface iron on the zeolites to promote the Fenton reaction. The biological assessment included measurement of the reactive oxygen species by flow cytometry and chemiluminescence techniques upon phagocytosis of the minerals. The chemical assessment included measuring the hydroxyl radicals generated from hydrogen peroxide by iron bound to the zeolite particles and fibers (Fenton reaction). Chromatography as well as absorption spectroscopy were used to quantitate the hydroxyl radicals. We found that upon exposure to the same mass of a specific type of particulate, the oxidative burst increased with decreasing particle size, but remained relatively independent of zeolite composition. On the other hand, the Fenton reaction depended on the type of zeolite, suggesting that the surface structure of the zeolite plays an important role. *Key words:* **erionite, faujasite, Fenton reaction, fiber toxicity, mordenite, zeolites.** *Environ Health Perspect* **110:1087–1096 (2002). [Online 12 September 2002]**
http://ehpnet1.niehs.nih.gov/docs/2002/110p1087-1096fach/abstract.html

Epidemiologic data suggest that environmental and/or occupational exposure to minerals, metals, and fibers can cause lung disease (*1–3*). These diseases typically develop over many years after exposure to the agents. The most studied fiber is asbestos (*1–3*). Man-made mineral or vitreous fibers can also be bioactive, though their role in respiratory disease in humans is not yet well established and is an active area of study (*4,5*). There are more than 70 varieties of synthetic inorganic fibers, covering over 35,000 applications, with different physicochemical and morphological characteristics. These include insulation materials (glass wool, rock wool, slag wool), glass filaments and microfibers, and refractory ceramic fibers (*4*). As a consequence of the extensive applications of these fibers, a significant fraction of the population is exposed. Thus it is essential to understand the basis of toxicity of respirable fibers. In this study, we focused on developing a better understanding of the biological and chemical reactivity of aluminosilicate fibers and particles.

Epidemiologic and experimental data have demonstrated that exposure to asbestos can induce pulmonary inflammation, fibrosis of the lower respiratory tract (asbestosis)(*1–3,6*) and is a risk factor for developing bronchiogenic carcinoma and mesothelioma (*7*). Numerous studies have been performed over the past 30 years to determine the mechanism(s) by which asbestos causes disease, and several hypotheses have been generated (*8*). Activation of macrophages by phagocytosis of the fibers results in the formation of reactive oxygen species (ROS) (*1–3,6,9,10*), where ROS is a collective term that includes radicals (superoxide anion, hydroxyl, peroxyl, and alkoxyl radicals), and hydrogen peroxide (H_2O_2). Iron bound to the fibers can generate hydroxyl radicals via the Fenton reaction, which can initiate lipid peroxidation, resulting in the production of intermediates that oxidize intracellular proteins and DNA (*11,12*).

In this study, we focused on separating the biological response (oxidative burst) and the chemical reactivity (Fenton reaction) using aluminosilicate crystals belonging to the zeolite family. There are several reasons we chose to examine zeolites as model systems. Even though the exposure of zeolites to the general population is quite limited, with possibly the exception of detergents, there is a particular zeolite called erionite that is highly toxic and causes mesothelioma (*13,14*). Several other zeolites have also been examined for their toxicity, but none so far has paralleled the effects of erionite. Erionite is a naturally occurring zeolite mineral that is far more carcinogenic than crocidolite asbestos (*13,15*). The framework of erionite is made up of interlocking tetrahedra of silicate and aluminate tetrahedra, is negatively charged, and can bind cations. The toxicity of natural erionite is commonly associated with the iron that accumulates on its surface after it is deposited within the respiratory epithelium (*16,17*). Mordenite is a natural zeolite with a chemical composition similar to erionite, as well as ion exchange abilities and to some extent a fibrous morphology. It is not reported to be carcinogenic and has been classified as being "slightly biologically active"(*17,18*).

In this study, we examined three zeolites, two of which are mineral zeolites, erionite and mordenite, and zeolite Y, a synthetic zeolite, extensively used as a catalyst. The biological response and surface chemical reactivity of the zeolites have been studied. For assessment of biological response, we examined the oxidative burst as a result of phagocytosis by rat pulmonary alveolar macrophage-derived cells (NR8383). We chose these cells because they can be propagated *in vitro* and exhibit a number of important macrophage characteristics, such as surface Fc receptors, interleukin-1 production and secretion, and oxidative burst response (*19*). Our previous studies dealt with phagocytosis of erionite by the NR8383 macrophages (*20,21*).

For determining chemical reactivity, we focused on the ability of the iron-exchanged forms of the zeolites to produce hydroxyl radicals from H_2O_2 (Fenton reaction). Both the intracellular and extracellular release of ROS by means of flow cytometry and chemiluminescence was studied. To distinguish cellular responses induced by fiber interactions with

Address correspondence to P.K. Dutta, Department of Chemistry, The Ohio State University, 100 West 18th Avenue, Columbus, OH 43210-1185 USA. Telephone: (614) 292-4532. Fax: (614) 688-5402. E-mail: dutta.1@osu.edu

We thank R. Kristovitch and H. Lee for assistance with some of the measurements. We thank the reviewers for helpful comments, especially regarding the role of surface area versus size.

Funding was obtained from The Ohio State University and the National Science Foundation (CHE- 0089147).

Received 15 October 2001; accepted 29 March 2002.

the plasma membrane from those induced by phagocytosis, we treated subsets of cells with the endocytosis inhibitor ammonium chloride. For surface chemical reactivity, we focused on the ability of the zeolites to promote Fenton chemistry. Total exchanged iron was quantified by elemental analysis, and surface iron was determined by a novel method utilizing the ion-exchange of surface iron by a positively charged polymer. To quantify the production of hydroxyl radicals, we used DMSO as a trapping agent. Its decrease was monitored by reverse phase liquid chromatography (RPLC) and by the formation of methanesulfinic acid (MSA), a stable product of the reaction of DMSO with hydroxyl radicals by electronic spectroscopy. Conclusions regarding the dependence of the oxidative burst on particle size and zeolite composition and the role of the zeolite surface structure on the Fenton chemistry are presented.

Materials and Methods

Cell Culture

The rat pulmonary alveolar macrophage-derived cell line, NR8383, was obtained from R. J. Helmke (University of Texas, Health Science Center, San Antonio, TX). The cells were cultured in Hams F12 medium (Sigma, St. Louis, MO) supplemented with 15% fetal bovine serum (Sigma) at 37°C in a humidified atmosphere of 5% CO_2 in 30-mL polystyrene culture flasks (Costar, Cambridge, MA). Cell populations were expanded by weekly passage at a ratio of 1:2. We determined cell viability by trypan blue exclusion.

Zeolite Characterization

Size fractionation. Approximately 1 g of mordenite or erionite (Minerals Research, Clarkson, NY) was added to 140 mL of water in 150-mL beakers, and allowed to settle for 70 and 96 min, respectively (determined by fiber density). The supernatant was then removed, filtered under vacuum through a 0.80 μm pore size filter and dried in an oven at 70°C. Zeolite Y obtained from Union Carbide (Danbury, CT) did not require size fractionation. We determined particle sizes of the fractionated materials by scanning electron microscopy (SEM). Diffraction patterns were collected using a Rigaku Geigerflex D/max2B diffractometer (Rigaku, The Woodlands, TX) using Ni-filtered CuKα radiation or a Bruker AXS D8 Advance diffractometer (Bruker AXS, Madison, WI) equipped with a rotating tilted sample holder. X-ray diffraction pattern peaks were search-matched using Jade 5 matching software (Materials Data, Inc., Livermore, CA).

Incorporation and determination of iron on zeolite. We placed 1 g of ground zeolite in a 12-mL centrifuge tube, to which 10 mL of a 0.1 M NaCl (Fisher Chemicals, Fair Lawn, NJ) solution was added. The suspension was sonicated for 15 min, shaken on a wrist shaker for 15 min, centrifuged, and the supernatant removed. This step was repeated twice. We deoxygenated solutions of 10^{-4}, 10^{-2}, 5×10^{-2} and 10^{-1} M iron sulfate heptahydrate (Sigma) with bubbling N_2 for 30 min and acidified them to pH 4 by adding concentrated hydrochloric acid (Fisher). Zeolite samples were added to the iron solutions and the suspensions shaken for 2 hr. After filtering, the zeolites were rinsed with deoxygenated water 6–10 times under N_2 atmosphere. We analyzed rinse waters by inductively coupled plasma-optical emission spectroscopy (ICP-OES) and a spectrophotometric method to ensure complete removal of adsorbed iron. Samples were dried overnight under a flow of nitrogen. ICP-OES experiments were done on the solutions obtained from lithium metaborate fusion of the zeolites and analyzed for iron (emission lines at 238.204, 239.562, 259.939, and 234.349 nm), aluminum (396.153, 308.215, 394.401, and 237.313 nm) and silicon (251.611, 212.412, 288.158, 252.851, and 221.667 nm) using an Optima 4300DV instrument (Perkin Elmer, Shelton, CT). Molybdenum was used as an internal standard at 5 ppm (emission lines at 202.03, 203.844, and 204.598 nm).

Spectrophotometric determination of solution iron. This method has been described by Fritz and Schenk (*22*). Solutions of 5 mM phenanthroline (Aldrich, Milwaukee, WI), 0.3 M ascorbic acid (Aldrich), and 1 M sodium acetate (Jenneile, Cincinnati, OH) were prepared in deionized water. The spectra were measured with a Shimadzu UV 265 or a Shimadzu UV-2501PC spectrophotometer (Shimadzu, Columbia, MD). Standards were prepared with iron sulfate.

Polymer exchange for surface iron determination. We used the polymer Dab-4Br, first described by Daniels et al. (*23*) and obtained by synthesis of 1,4-diazabicyclol [2.2.2] octane (Dabco) with $Br(CH_2)_4Br$. Solutions of 0.5 g of Dab-4Br in 40 mL water were prepared, and 8 mL of this solution was added to 0.4 g of dried iron-exchanged zeolite samples in a 12-mL centrifuge tube. The mixture was placed on a wrist shaker for 20, 40, or 60 hr. We then centrifuged the solutions and analyzed them for iron.

Diffuse reflectance. UV-Vis diffuse reflectance spectra were acquired on a Perkin Elmer Lambda 900 UV-Vis-NIR spectrometer. We used Kubelka-Munk units. The reference sample was the unexchanged zeolite.

Cell–Particle Interactions

We obtained the fluorescent dye 5- (and 6-) carboxy-2′,7′-dichlorodihydrofluorescin diacetate (H_2DCF-DA) from Molecular Probes (Eugene, OR). We divided 25 mg of H_2DCF-DA dissolved in 5.0 mL of anhydrous DMSO (Aldrich) into aliquots and stored them at –4°C in a freezer/desiccator until use. NR8383 cells were pelleted by centrifugation (400 × *g*, 10 min) and resuspended in fresh Hams F12 medium (~2.5×10^4 cells/mL). Cells were treated with H_2DCF-DA (final concentration 20 μM) and incubated for 20 min at 37°C in a humidified atmosphere of 5% CO_2. Zymosan A (Sigma), size-fractionated erionite, mordenite, and zeolite Y were each suspended in medium (100 μg/mL) and sonicated for 20 min immediately before addition to cells.

After incubation, we treated 1-mL aliquots of cells (2.5×10^4) with 1 mL of fiber suspension (100 μg particles/mL) in culture medium or in ACAS buffer [127 mM NaCl, 3.8 mM KCl, 1.2 mM $CaCl_2$, 5 mM glucose (Jenneile Chemical), 0.8 mM $MgCl_2$ (Mallinckrodt, Paris, KY), 1.2 mM KH_2PO_4 (J.T. Baker Chemical, Phillipsburg, NJ), and 10 mM HEPES (Sigma), pH 7.4]. For negative controls, we treated additional aliquots of cells with 1 mL of medium or buffer alone. To promote cell/fiber contact, cell suspensions were vortexed briefly (10 sec) then gently centrifuged (200 × *g*, 3 min). This cycle was performed three times, after which cells were analyzed as described below.

To distinguish cellular responses induced by fiber interactions with the plasma membrane from those induced by phagocytosis, we incubated subsets of cells for 1 hr in medium supplemented with the endocytosis inhibitor NH_4Cl (Mallinckrodt), at a final concentration of 20 mM. Cells were then washed and resuspended in fresh NH_4Cl-supplemented medium before treatment with particulates.

Flow cytometry. Flow cytometric analysis was performed on a Coulter Epics Elite flow cytometer (Beckman Coulter Inc., Miami, FL) equipped with a 15-mW air-cooled argon ion laser (Cyonics, San Jose, CA) operating at 488 nm. Fluorescence emission was collected using a 525-nm band pass filter. We measured the uptake of particulates by viable cells (determined and gated from a bivariate histogram of right-angle light scatter versus forward-angle light scatter) by the increase in the right-angle scatter signal as displayed on a univariate histogram of right-angle scatter versus the number of events. We used the mean right-angle scatter channel number for data analysis, as well as the mean fluorescence intensity and percentage of cells exceeding values measured for untreated control populations.

Chemiluminescence assay. Luminol (Sigma) was dissolved in DMSO at a concentration of 10 mM and stored in aliquots at –4°C. Just before use, luminol was thawed and diluted to 100 μM in phosphate-buffered saline (PBS), with a resultant final concentration of 1%. Zymosan A (Sigma), size-fractionated erionite,

mordenite, and zeolite Y were each suspended in PBS at concentrations of 5.0, 1.0, and 0.2 mg/mL and sonicated for 20 min immediately before treatment of cells. NR8383 cells were pelleted by centrifugation (400 × *g*, 10 min) and resuspended in fresh Hams F12 medium (1.0×10^6 cells/mL).

We performed luminescence reactions in 96-well black Optiplates (Packard, Meriden, CT). To each well we added 100 µL of luminol (final concentration in total volume of well was 40 µM), 50 µL of fiber suspensions (250 µg, 50 µg or 10 µg/well), and 100 µL of cell suspension (1×10^5 cells/well, added last to synchronize kinetics among reactions). All reactions were performed in duplicate. As controls, each experiment also included duplicate wells containing luminol alone, cells alone, or cells and luminol but no fibers. Plates were sealed and luminescence was immediately measured with a Top-Count Microplate Scintillation and Luminescence Counter (Packard). After this initial measurement, plates were centrifuged (400 × *g*, 1 min) to promote fiber/cell contact. We subsequently performed luminescence measurements at 3-min intervals over 2 hr. Plates were kept in an incubator at 37°C between each measurement.

To distinguish cellular responses induced by fiber interactions with the plasma membrane from those induced by phagocytosis, we incubated subsets of cells for 1 hr in medium supplemented with 20 mM NH_4Cl before use in experiments, and all components of reactions were likewise supplemented to attain a final NH_4Cl concentration of 20 mM in reaction wells. We obtained corrected chemiluminescence curves by subtracting values generated by negative control reactions (cells plus luminol in the absence of fibers) from those generated under each experimental condition. We then calculated total luminescence values by integration of the area under each corrected chemiluminescence curve (Grams/32 program; Thermo Galactic, Salem, NH).

Transmission electron microscopy. To determine the effectiveness of the endocytosis inhibitor NH_4Cl, we incubated NR8383 cells for 1 hr in culture medium in the presence or absence of 20 mM NH_4Cl, then exposed cells to erionite or mordenite using the vortex/centrifugation method described above. Cells were fixed, embedded, sectioned, and imaged by transmission electron microscopy as previously described (*21*).

Hydroxyl Radical Measurements

Reverse-phase liquid chromatography. We used a Waters C18 Resolve1 10 µm column (8 mm × 10 cm; Waters, Milford, MA) and a Shimadzu LC-10ATVP HPLC system coupled to an SPD-M10AVP diode array detector (Shimadzu). The injection volume was 20 µL. The eluant consisted of 5% methanol in nanopure water, filtered through a Duropore filter and degassed the day of use. We used an isocratic flow of 1 mL/min. The sample loop was rinsed six times with the sample and flushed six times with eluant after injection. All samples were injected in triplicate. Four standards of DMSO/H_2O_2 solutions were run. Integration of the peak areas was performed using Grams/32 software.

We added 10 mL of a 0.384 mM H_2O_2 and 0.939 mM DMSO solution to the dried iron-exchanged zeolite, and the mixture was shaken for 30 min on a wrist shaker. The solution was then centrifuged, and a fraction of the supernatant was filtered and injected into the chromatographic system. Centrifugation was performed using a Beckman-Coulter Alegra 64R centrifuge at 25,000 rpm for 10 min. To determine the influence of any iron released from the zeolite into solution, 2 mL of the last rinse solution was added to 10 mL of the H_2O_2/DMSO mixture, shaken for 30 min, and examined by chromatography.

Spectrophotometric determination of methanesulfinic acid formation. Babbs and Steiner (*24,25*) developed the spectrophotometric quantification of MSA, and we used a modified version of this method. The photooxidized species from the Fast Blue BB salt solution $(C_{17}H_{18}ClN_3O_3)ZnCl_2$ (Fluka Chemie; Sigma-Aldrich USA, Milwaukee, WI) was removed by extraction with 1 mL chloroform. We added 0.3 mL of 1N HCl and 0.2 mL of 0.02 M Fast Blue BB salt solution to 2.0 mL of sample (obtained after zeolite treatment with DMSO and H_2O_2). The tube was kept in the dark for 10 min. We added 1.5 mL of a solution of toluene-butanol 3:1, and then the mixture was vortexed for 120 sec and centrifuged. We then removed 1.0 mL of the organic phase, placed it in a second tube, and added 2.0 mL of butanol-saturated water. The mixture was vortexed 30 sec and centrifuged briefly. We removed 0.9 mL of the upper phase and placed it in the UV cuvette, along with 1.5 mL of the butanol-toluene 3:1 solvent. Spectra were recorded on a Shimadzu UV 265 or a Shimadzu UV-2501PC spectrophotometer, from 500 to 330 nm. We used 2.4 mL of the 3:1 mixture of toluene-butanol as a blank. Standards were run by repeating this procedure with solutions of 0.01 mM to 0.15 mM of MSA (obtained from Lancaster Laboratories, Pelham, NH).

Results

Physical Characteristics of Zeolites

The powder diffraction patterns depicted in Figure 1 compare well with previously published data on all three samples (*26*). For erionite, the peaks at 2θ values of 12.2° and 38.0° match the characteristic peaks of calcium aluminum silicate hydrate ($Ca_4Al_8Si_8O_{32}\cdot 8H_2O$), and the peaks at 12.2°,17.5°, and 55.9° most likely belong to sodium aluminum silicate hydrate ($Na_3Al_3Si_5O_{16}\cdot 6H_2O$). No extraneous phases were evident in the X-ray diffraction pattern of mordenite and zeolite Y.

Size fractionation results were analyzed by means of SEM, and the data for erionite and mordenite are shown in Figure 2. Scanning electron micrographs of an erionite dispersion before and after fractionation (Figure 2A,B) show that the average length and width of the fibers has effectively decreased, as well as the size range. The unfractionated erionite sample includes long fibers, up to 45 µm, with a mode (most frequent length) of approximately 10 µm. Fractionation of this sample led to a population ranging from 0.7 µm to 13 µm, with a mode of about 3 µm, the fiber morphology appearing intact.

Fibrous morphology on mordenite was not frequently observed. Depending on the geographic source of mining, mordenite may

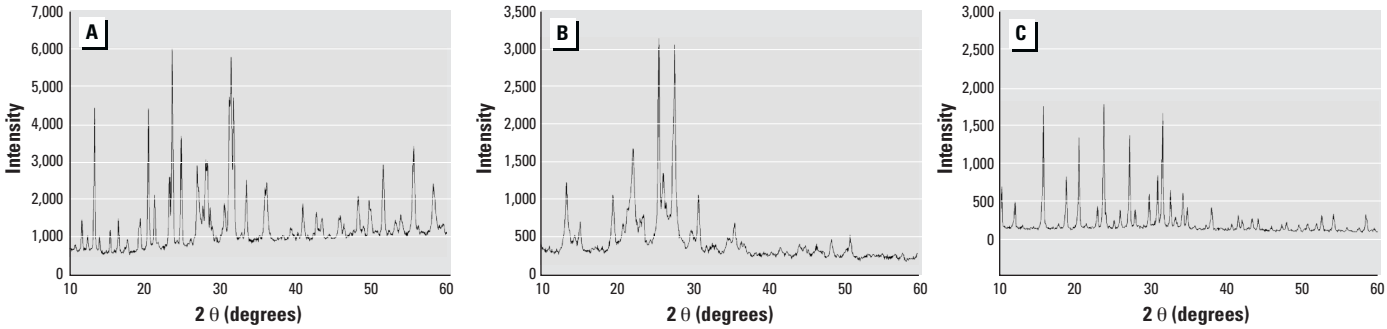

Figure 1. Powder X-ray diffraction patterns of (*A*) erionite, (*B*) mordenite, and (*C*) zeolite Y.

not be fiber-shaped (*27,28*). We observed that unfractionated mordenite particles range from 0.1 to 10 µm, with a mode of approximately 3.7 µm. Size fractionation of mordenite allowed discrimination against the largest particles, as well as particles smaller than 1 µm. The most abundant size observable on the SEM is centered on the value of approximately 1 µm. Zeolite Y appeared as octahedral crystals of a homogeneous size of slightly less than 1 µm (Figure 2E).

Cell–Fiber Interactions

Morphologic characteristics of fiber-treated cells. Morphologic characteristics of cells determine their light-scattering properties (*29*). The amount of light refracted in a forward direction (forward angle light scatter) is proportional to cell size and the refractive index of the cytoplasm. In contrast, the amount of light reflected at right angle (side scatter) is largely determined by the intracellular morphology of the cell, such as differences in nuclear size or shape, cytoplasmic granules or vacuoles, or bound particles. By plotting the side-scatter versus forward-scatter signals of cells in suspension, it is possible to distinguish single viable cells from nonviable cells (based on differences in refractive index) and cell clusters (based on differences in cell volumes). To show whether cells had phagocytized zeolite particles, side scatter was plotted only for the living cell population. The mineral suspensions alone showed a small forward-scatter and a relatively wide side-scatter range but did not overlap with the living cell population.

Side scatter increased with time of exposure to particles, so samples were analyzed exactly 20 min after exposure to particles. Table 1 presents the side-scatter increase for cells exposed to the three minerals. For zeolite Y, the increase was 25%. Erionite particles induced a large increase in side scatter, with an average increase of 58%. Mordenite induced the second largest increase, reaching a value of 41%. In all cases, smaller particles, obtained via fractionation or sonication, induced a smaller increase in side scatter than their corresponding larger counterparts.

NH_4Cl was used as the endocytosis inhibitor to inhibit association of the macrophages with particulates (*30*). Cell viability, evaluated using trypan blue after 1-hr exposure to NH_4Cl-enriched medium, was unaltered as compared to a blank. Cells treated with NH_4Cl and exposed to fractionated erionite, fractionated mordenite, and zeolite Y all showed relative increase in side scatter that was only about 75% of that observed in cells exposed to particles in the absence of inhibitor (Table 1).

Oxidative burst. We measured the oxidative burst as both the mean fluorescence intensity generated by viable cell populations and the percentage of cells with fluorescent intensities above the background level of untreated controls. A large positive signal was reproducibly observed in the case of zymosan for three replications. A typical result was that the percentage of cells generating fluorescent signal in excess of untreated controls increased from 4% to 53% of the total viable cell population upon exposure to zymosan, and the mean fluorescence intensity increased approximately 13-fold. However, despite extensive efforts, flow cytometry did not exhibit significant increase in fluorescence after exposure of the cells to the three different minerals. We attempted various modifications, including use of a different fluorochrome (dihydrorhodamine123), variation of exposure time, and modification of the centrifugation/vortex protocol, but all failed to induce a detectable oxidative response from the cells.

Figure 3 shows a typical response of the luminol chemiluminescence induced by superoxide generated by mordenite-stimulated cells as a function of time. For all three zeolites, the peak luminescence occurred between 20 and 25 min after exposure. Table 2 summarizes the integrated chemiluminescence results generated by NR8383 cells treated with various concentrations of each of the three minerals. These data demonstrate dose-dependent responses in all cases: the greatest luminescence signal was always associated with the highest mineral concentration. Figure 4 illustrates the dose response observed for fractionated mordenite, rising from 946 ± 139 (10 µg) to 8382 ± 1,855 (250 µg). In addition, we observed that for exposure to the same mass of particulates, the chemiluminescence signal was inversely correlated with particle size for each category of zeolites. Figure 5 presents the results obtained with three different size fractions of erionite, including a fraction of erionite called "fine erionite" (ranging from 0.2 µm to 4 µm, with a mode of 0.8 µm, as determined by SEM), all at a dose of 50 µg.

To distinguish cellular responses induced by fiber interactions with the plasma membrane from those induced by phagocytosis, we treated subsets of cells with the endocytosis inhibitor NH_4Cl. Chemiluminescence

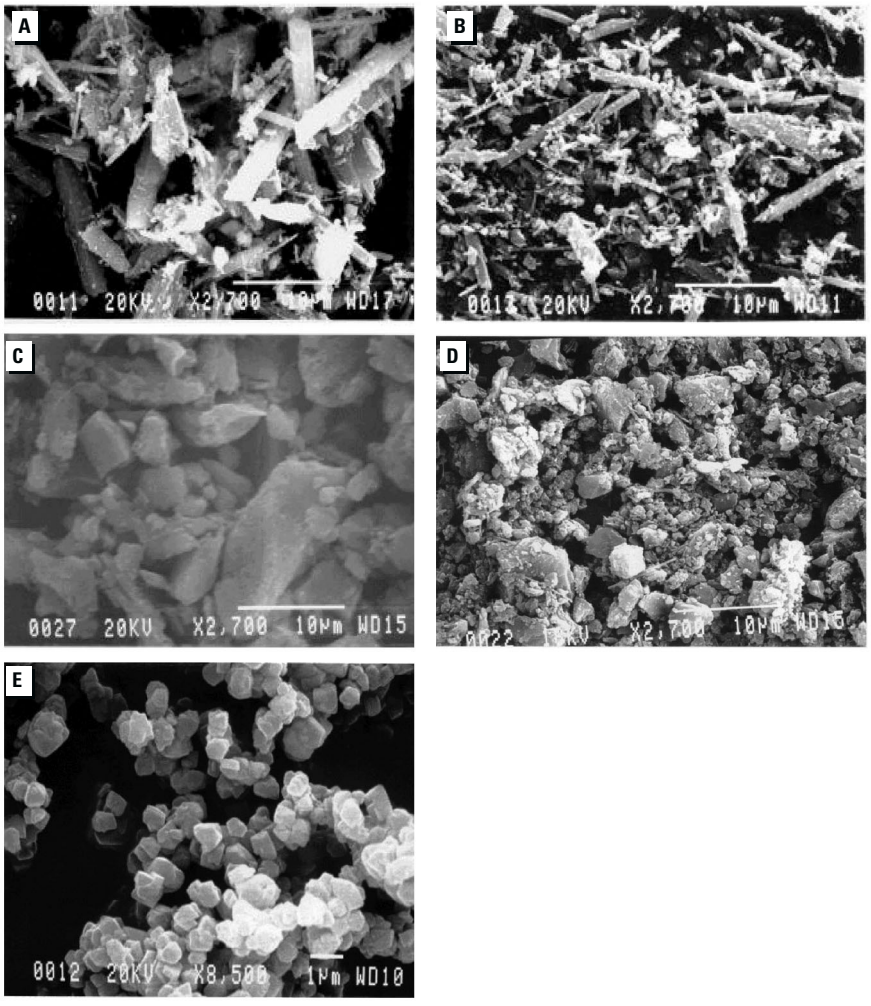

Figure 2. Scanning electron micrographs of zeolites. Erionite (*A*) before and (*B*) after size fractionation. Mordenite (*C*) before and (*D*) after size fractionation. (*E*) As-synthesized zeolite.

assays of responses of NH_4Cl-treated cells after exposure to fibers demonstrated that inhibition of endocytosis dramatically attenuated oxidative burst intensity, with typically about 70% reduction in levels of chemiluminescence. Although absolute levels of luminescence were reduced, NH_4Cl-treatment had little effect on the kinetics of fiber-induced oxidative burst. These data suggest that fiber-induced ROS production is primarily dependent on fiber phagocytosis, rather than fiber–membrane interactions.

Electron microscopy. Transmission electron microscopy of untreated and NH_4Cl-treated cells followed by exposure to erionite or mordenite are shown in Figure 6. The micrographs suggest that, although NH_4Cl treatment did not affect binding of fibers to the plasma membrane, it reduced the quantity of intracellular fibers from about eight per cell (untreated) to one to two per cell (NH_4Cl-treated) (based on a study of four micrographs).

Chemical Studies

Bulk and surface iron analysis. Table 3 summarizes the total and surface-exchanged iron of the zeolites exposed to different concentrations of iron sulfate solutions, as determined by ICP-OES and the polymer exchange method, respectively. Mordenite, erionite, and zeolite Y had initial levels of total iron of 4.7×10^3, 12.7×10^3, and 0.35×10^3 μg iron/g of zeolite, respectively. Levels of total iron in erionite dropped from 12.7×10^3 to 10.3×10^3 μg iron/g and for mordenite from 4.7×10^3 to 3.6×10^3 μg iron/g after sodium ion exchange, indicating that the iron is either part of the framework or present as an impurity phase. The iron levels on as-synthesized zeolite Y were the lowest. An increase in concentration of iron in solution resulted in an increase of the total exchanged iron. As expected from exchange isotherms (*31*), this increase is not linear and tends to level off at higher concentrations. Surface areas (BET; Brunauer, Emmett, and Teller) of 86 m^2/g, 295 m^2/g, and 518 m^2/g were determined for mordenite, erionite, and zeolite Y, respectively. Mordenite has the lowest surface area because of structural defects that block the channels, and for this reason it is also the poorest ion-exchanger of the three zeolites.

The spectrophotometric method to determine surface iron content is based on back-exchange of iron by a charged cationic polymer, Dab-4Br. The released iron after 20, 40, and 60 hr were measured and found to level out after 40 hr. We therefore report the results as the levels of iron exchanged after 40 hr of ion-exchange. To confirm that the polymer was exchanged only at the zeolite surface, we monitored the X-ray photoelectron spectroscopy before and after exposure. These studies showed a decrease in the Fe/Si ratio; however, the iron signal did not fully disappear. We attribute this to signal from the bulk iron, since X-ray penetration depth is approximately 50 Å. The small standard deviations for surface iron levels indicate good reproducibility of the method. Surface iron increases with the concentration of the initial iron solution, ranging from 1.4 μg/g to 12.3 $\times 10^2$ μg/g for zeolite Y, from 5 μg/g to 4.0 $\times 10^2$ μg/g for mordenite, and from 1.6 μg/g to 3.3 $\times 10^2$ μg/g for erionite. Levels of surface iron in natural samples before any exchange are 30 μg/g and 4 μg/g for mordenite and erionite, respectively, values that drop to undetectable levels after sodium exchange.

The large increase of surface iron on zeolite Y when exposed to iron sulfate solutions of 0.1 M was examined further. The pH of the initial solution of acidified iron sulfate was 3. X-ray diffraction patterns of the zeolite Y after exposure to these solutions confirmed a loss in crystallinity, whereas the structure was stable for both erionite and mordenite. The lower Si/Al ratio of zeolite Y makes it more prone to degradation (*31*). Consequently, the value of 12.3 ± 0.3 $\times 10^2$ μg of surface iron/g of zeolite Y represents iron exchanged onto the zeolite and also incorporated into the amorphous material.

Diffuse reflectance spectroscopy. UV-Vis diffuse reflectance spectra were recorded on the three iron-exchanged zeolites (Figure 7). A peak at 240–250nm, as well as a band at 220 nm, was observed for all three zeolites. The peak at 290 nm is present in erionite and zeolite Y but does not appear on the mordenite spectrum. Mordenite exhibits a small absorption band 320 nm, which appears also in the erionite spectrum but is nonexistent in the zeolite Y spectrum. Finally, mordenite also exhibits a small absorbance at 450 nm. The common peak at 240–250 nm may be assigned to the charge transfer transition between the oxygen atoms and the framework iron species (*32*), which explains why it

Table 1. Side-scatter increase upon cell–particle interaction with and without NH_4Cl treatment of the macrophages.

	Side-scatter increase (%)	
	Without NH_4Cl	With NH_4Cl
Erionite	58 ± 8	NA
Fractionated erionite	33	24
Mordenite	41 ± 0.2	NA
Fractionated mordenite	24 ± 3	18
Zeolite Y	25	20

NA, not analyzed. SDs are the result of two or more measurements.

Table 2. Integrated chemiluminescence intensity upon macrophage–particle interaction (arbitrary units).

	Median size (μm)	10 μg	50 μg	250 μg
Mordenite	3.7	NA	503 ±183	649 ± 303
Fractionated mordenite	1	946 ± 139	1,846 ± 1,134	8,382 ± 1,855
Erionite	10	NA	695 ± 288	1,166 ± 589
Fractionated erionite	3	NA	965 ± 361	1,110 ± 333
Fine erionite	0.8	NA	1,904	NA
Zeolite Y	0.9	611	1,359 ± 1,133	3,909 ± 1,340

NA, not analyzed. SDs are the result of two or more measurements.

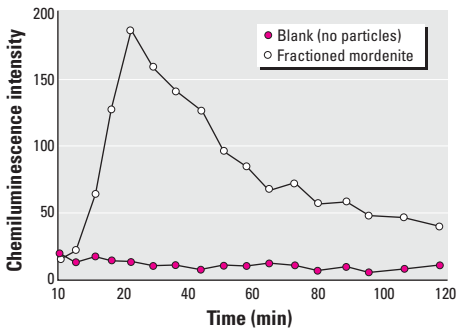

Figure 3. Luminol-based chemiluminescence data after exposure of NR8383 cells to fractionated mordenite (50 μg).

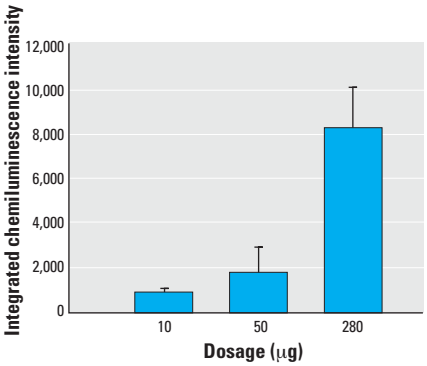

Figure 4. Comparison of the levels of chemiluminescence from different dosages (10, 50, 250 μg) of fractionated mordenite.

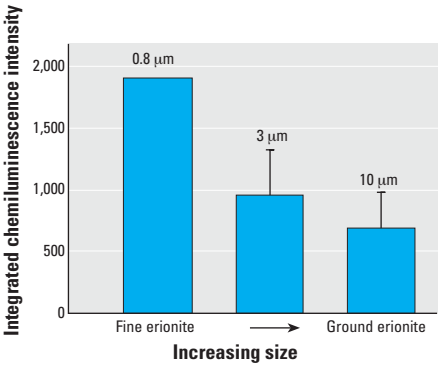

Figure 5. Comparison of the levels of chemiluminescence as a function of particle size, using erionite as the sample.

is almost nonexistent in the case of zeolite Y, which does not have any framework iron. Tuel et al. (*33*) assigned the 220-nm band in iron-containing mesoporous silicas to a ligand-to-metal charge transfer that involves isolated, tetrahedrally coordinated Fe^{3+}. The peak at 295 nm is of particular interest because it is present in the case of erionite and zeolite Y but does not appear in the mordenite spectrum. Conversely, mordenite exhibits a small absorption band at 320 nm, which also appears in the erionite spectrum but is nonexistent in the zeolite Y spectrum. This band region has been correlated with spin-forbidden d-d transitions in Fe-silicalite (*34*). Finally, the small absorbance of mordenite at 450 nm may be indicative of impurity iron oxides.

Fenton chemistry. The redox state of iron is relevant for Fenton-type reactions because iron(II) is necessary to initiate this reaction. Although the Haber-Weiss cycle allows the reduction of iron(III) by reducing agents (e.g., superoxides), we ensured that our sample began with iron in the +2 state. Therefore, we started with ferrous sulfate salts and used caution to keep iron in this redox state, following procedures given by previous researchers (*35*).

We used two methods to analyze for the hydroxyl radicals. The difference in the amount of DMSO before and after reaction with hydroxyl radicals was estimated from liquid chromatography. The second method involved UV-visible spectroscopy for estimating MSA formed by reaction of hydroxyl radicals with DMSO, and a detection limit of 100 µmol of MSA was achieved (*24,25*).

Figures 8 and 9 plot the amount of hydroxyl radicals by the HPLC and the UV-Vis methods, respectively, against the amount of surface iron determined by the polymer exchange method (micrograms iron per gram of zeolite times grams dry zeolite used for the experiment). For mordenite and erionite, the production of hydroxyl radicals increases as surface iron increases. Increasing amounts of surface iron on zeolite Y did not give rise to increasing production of hydroxyl radicals. Results obtained with fractionated mordenite samples are similar to those with unfractionated mordenite for similar iron loading levels (data not shown). For similar amounts of surface iron, and especially at the higher surface iron levels, erionite induced a larger hydroxyl radical production than mordenite, which induced a larger production than zeolite Y. The data obtained with free iron in solution show a relatively small production of hydroxyl radicals (7.3×10^{-5} mmol for 350 µg iron).

Discussion

Measurement of the Oxidative Burst

The difference in results pertaining to the measurement of the oxidative burst between the chemiluminescence and the flow cytometry techniques can be rationalized as follows. Chemiluminescence technique provides a measure of H_2O_2, $OH^{\bullet}$, $O_2^{\bullet-}$, whereas the flow cytometry, though supposedly specific to H_2O_2, has been shown recently to be sensitive to a variety of reactive oxygen species, including superoxides (*36,37*). In addition, it is known that the rate of spontaneous $O_2^{\bullet-}$ dismutation into H_2O_2 is rapid, either spontaneously or by the enzyme superoxide dismutase. Therefore, the measurement of different oxygen species is not the cause for the differences in results. An examination of the reported detection limits for the chemiluminescence and flow cytometry method provide a better explanation. For the NR8383 cell line, Helmke et al. (*19*) reported 4×10^{-9} M $H_2O_2/5 \times 10^5$ cells after exposure to zymosan, which corresponds approximately to 10^{-17} mol of H_2O_2 per cell. Since 100,000 cells are present in the chemiluminescence system, this would correspond to 10^{-12} mol of H_2O_2 generated, or a 10^{-6} M concentration (well volume is 250 µL). The signal from zymosan is 10–100 times higher than the mineral-induced signals, which would set the concentration of hydrogen peroxide generated upon mineral stimulation in the 10^{-8} to 10^{-7} M range. Detection limits have been reported for chemilumenescence in the 10^{-8} M range of concentrations for H_2O_2 (*38*), which is consistent with the detection of responses from mineral-challenged cells. In flow cytometry, the signal detected per cell has been reported to be 10^{-17} mol of oxidized fluorescein dye per cell (*39*) and is in the range generated upon zymosan stimulation. However, the H_2O_2 generated by exposure to minerals is several orders magnitude lower

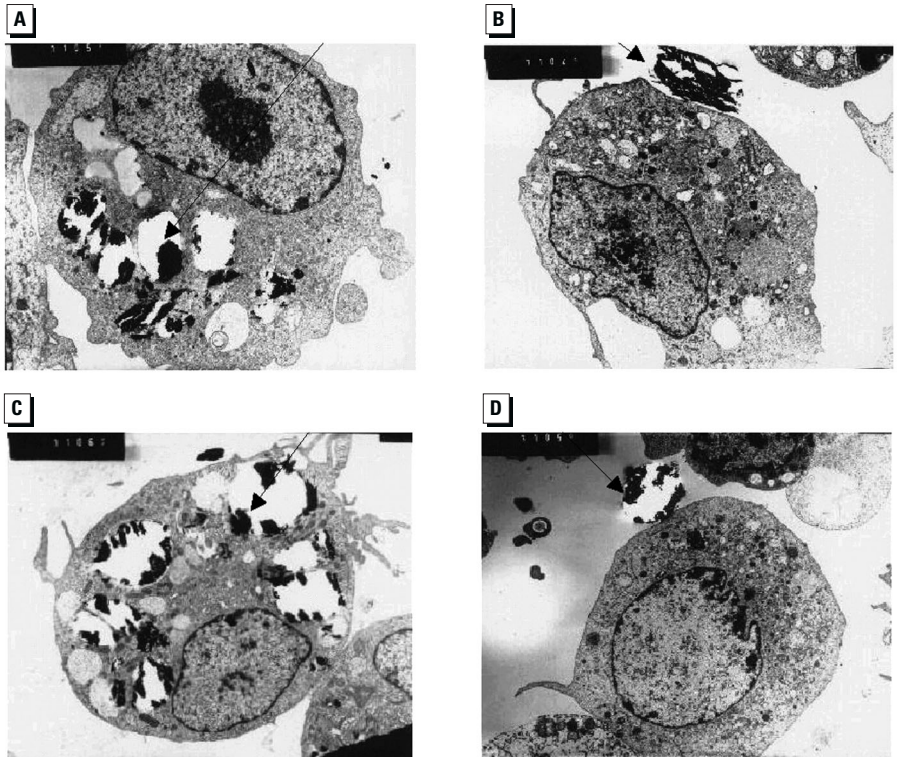

Figure 6. Electron micrographs of NR8383 cells exposed to erionite (*A,B*) and mordenite (*C,D*) before treatment (*A,C*) and after treatment (*B,D*) with the endocytosis inhibitor NH_4Cl. Arrows indicate erionite particles (*A,B*) and mordenite particles (*C,D*).

Table 3. Total and surface Fe content for the natural, sodium-preexchanged and iron-exchanged zeolites (acidified solutions of 10^{-4}, 10^{-2}, 5×10^{-2}, and 10^{-1} M of $FeSO_4 \cdot 7H_2O$).

	Mordenite		Erionite		Zeolite Y	
	Total ($\times 10^3$)	Surface ($\times 10^2$)	Total ($\times 10^3$)	Surface ($\times 10^2$)	Total ($\times 10^3$)	Surface ($\times 10^2$)
Natural	4.7	0.3	12.7	0.04	0.35 ± 0.05	ND
NaCl-exchanged	3.6 ± 0.2	ND	10.3	ND	0.092	ND
10^{-4} M Fe	3.7 ± 0.7	0.05	5.6	0.016	0.45 ± 0.08	0.014
10^{-2} M Fe	4.16 ± 0.53	1.9	18 ± 3	1.6 ± 0.4	7 ± 1	0.024 ± 0.004
5×10^{-2} M Fe	11.3	NA	NA	NA	18 ± 1	2.97
10^{-1} M Fe	11.6	4.0 ± 0.2	25	3.3 ± 0.4	34 ± 1	12.3 ± 0.3

Abbreviations: NA, not analyzed; ND, not detected. Results are expressed as micrograms iron per gram of zeolite. SDs are the result of two or more experiments.

than that induced by zymosan and therefore below the detection limit of flow cytometry.

Phagocytosis and the Oxidative Burst

The three issues that we have discussed are cell viability upon exposure to the zeolites, the origin of the oxidative burst, and the magnitude of the oxidative burst for the three samples. A calculation of the number of particles in 250 μg of zeolite Y, based on a density of 2.3 g/cm^3 and a radius of 0.9 μm (assuming a spherical shape) gives rises to an estimated value of 300 particles/cell. Although this number is high, cell viability is retained: Light microscopy showed similar numbers of living cells before and after exposure to particles. Furthermore, previous researchers have shown that a decrease in cell viability could be detected by a rapidly decreasing chemiluminescence signal, returning to baseline signals faster than in healthier cell systems (*40*). Such a phenomenon would be more likely to happen at higher fiber dosage. We have not observed a more rapidly decreasing signal at 250 μg dosages when compared to the 10 μg dosage. Therefore, cell viability is estimated to be similar for all three particles types and dosages in this time range.

We also have addressed the issue of the signal appearing from phagocytosis versus just membrane binding. For all three zeolites, the chemiluminescence peak typically occurred between 20 and 25 min and corresponds to the maximum in the oxidative burst. Nadeau et al. (*40*) observed that the time at which the maximum chemiluminescence signal is obtained is inversely related to dosage. Urano et al. (*41*) claimed that the earlier peaks could be reflecting faster kinetics in the superoxide generating process due to erionite fiber–membrane interaction rather than phagocytosis. In the present study, the time at which the peak maximum occurred did not vary after treatment of the cells by NH_4Cl. The decrease in the side scatter after treatment of the cells by the endocytosis inhibitor shows that phagocytosis is decreasing. This is consistent with the 70% decrease in chemiluminescence after treatment of the cells by ammonium chloride, suggesting that phagocytosis, rather than membrane interaction, is triggering the oxidative burst. These results correlate with the findings of Ng et al. (*30*). After addition of endocytosis inhibitors (chloroquine and ammonium chloride) to microsphere-exposed NR8383 cells, they observed no cell–microsphere interaction. They concluded that phagocytosis rather than simple binding caused the chemiluminescence signal. This phagocytosis-induced response of NR8383 cells, rather than a membrane response, is in accordance with the relatively small burst that Helmke et al. (*42*) obtained with phorbol myristate acetate (PMA) stimulation compared to zymosan-induced stimulation of NR8383 cells. They found a maximum 2-fold increase in the chemiluminescence signal after PMA stimulation, and an average 23-fold increase after zymosan stimulation. Because PMA-induced response is a membrane phenomenon, while zymosan activation involves phagocytosis, this suggests that NR8383 cells do not show a large oxidative burst upon membrane stimulation. We have observed that all mineral-induced responses were 10- to 100-fold smaller than the zymosan response, which is consistent with previous experiments. Ng et al. (*30*) reported small, dose-dependent signals of chemiluminescence upon uptake of polymeric microspheres by NR8383 cells, compared to the zymosan-induced chemiluminescence.

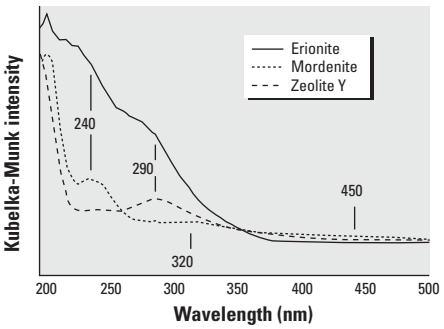

Figure 7. Diffuse reflectance spectra of Fe(II)-exchanged zeolites.

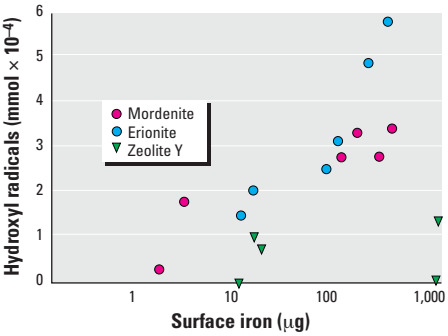

Figure 8. Production of hydroxyl radicals measured by chromatography of DMSO as a function of surface Fe(II) on different zeolites.

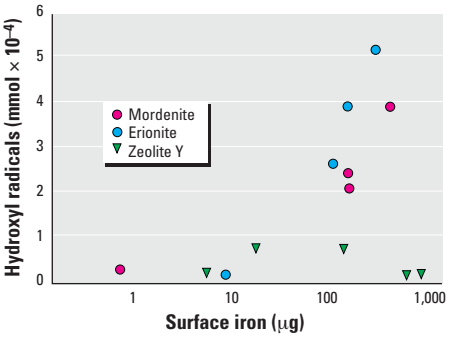

Figure 9. Production of hydroxyl radicals measured by UV-visible spectroscopy of MSA as a function of surface Fe(II) on different zeolites.

For the same mass loading of particulates, the signal from oxidative burst upon phagocytosis is inversely correlated with particle size, regardless of the nature of the zeolite (Table 2). Fractionated mordenite induces a larger oxidative response than unfractionated mordenite. Similarly, the third size fraction of erionite, "fine erionite," induced significantly larger response than fractionated erionite, whereas fractionated erionite induced a larger response than ground erionite, all at a dosage of 50 μg. Unfortunately, we do not know the number of particles in the cell upon exposure to samples with different particle sizes. If we assume that the same mass of particles is entering the cell, then there will be larger number of smaller particles per cell for the finer size and that would thus present a much larger surface area. In this case, it would imply that there is a positive correlation between the oxidative burst and the surface area of particles.

As far as the differences in the magnitude of the oxidative burst for the different particles, Table 2 suggests that for comparable sizes of the particles, there is no significant difference in the oxidative burst, especially between the minerals erionite and mordenite.

Fenton Chemistry at the Mineral Surface: Methodology

Both methods used to estimate hydroxyl radicals involve the reaction of $OH^{\bullet}$ with DMSO followed by either measurement of the remaining DMSO or the amount of the stable product, MSA. The reaction of hydroxyl radicals with DMSO has an appreciable rate constant ($k = 7 \times 10^9$ L/mol·sec), and the reported yield for this reaction varies from 85% to 91% (*24,25,43*). The MSA method gave somewhat lower values than the HPLC method, but the trends in both cases were similar. We believe that the MSA method is more accurate because it determines the amount of a product formed rather than measuring differences between the amount of the reactant.

To confirm that the Fenton chemistry is solely due to surface-bound zeolitic iron rather than the bulk, measurement of the MSA production was done on iron-zeolite that was treated with Dab-4 polymer. On these zeolites, surface iron is absent, and iron present only in the bulk. No MSA production was observed.

The concern that H_2O_2 and/or DMSO could diffuse into the zeolite cages and thereby exhibit a smaller signal in the HPLC method was examined by quantitatively estimating the levels of H_2O_2 and DMSO after exposure to iron-containing zeolites. In all three zeolites, there was no decrease in amount of H_2O_2. Erionite and mordenite showed no loss of DMSO, but zeolite Y did. This finding correlates well with dimension considerations: The kinetic diameter of DMSO is 5 Å, so it is size-excluded from erionite (pore windows 3.6 ×

5.1 Å) (*44*). DMSO can penetrate mordenite through the 6.5 × 7.0 Å windows, but the defect structure limits the porosity. Zeolite Y showed a decrease of $1.09 \times 10^{-4} \pm 3 \times 10^{-6}$ mmol of DMSO/g zeolite, and the data for the HPLC method were corrected for the pore trapping of DMSO. After correction, results comparable to the MSA method were observed.

Another concern was that iron released into solution from the zeolite was responsible for the Fenton chemistry. The released iron in solution after reaction with the DMSO/H_2O_2 solution was estimated spectrophotometrically (phenanthroline method). This method is less sensitive than ICP-OES, but this latter technique was not an option because colloidal zeolite could be present in solution. Approximately 5% of the surface iron was found to be in solution. Since the aqueous complexes of iron show a considerably smaller "Fenton activity" than zeolite-bound iron, we rule out the possibility that solution iron plays an important part in the radical production.

Other complications could involve reaction of methyl radicals with DMSO, leading to overestimation of the results obtained by the HPLC method. This reaction will not influence the MSA method. The rate constant between H_2O_2 and hydroxyl radicals, $k = 1.2 - 4.5 \times 10^7$ L/mol·sec, is smaller than the rate constant of OH• with DMSO ($k = 7 \times 10^9$ L/mol·sec) (*45*), thus, loss of hydroxyl radicals by reaction with H_2O_2 is not important. Ulanski et al. (*46*) studied the kinetics of reaction of methyl radicals with H_2O_2 and found a reaction rate of 2.7×10^4 L/mol·sec, which is slow enough not to be problematic.

Role of Zeolite Surface Structure in Fenton Chemistry

For mordenite and erionite, the production of hydroxyl radicals increases as surface iron increases. Experiments with fractionated mordenite show that although surface iron increases per gram of zeolite, its activity in the Fenton reaction normalized to surface iron levels is similar to unfractionated mordenite. For comparable amounts of surface iron, especially at the higher loadings, erionite induces a larger hydroxyl radical production than mordenite, which induces a larger production than zeolite Y. Though the mechanism of the Fenton reaction is still being debated (*47,48*), it is accepted that the ligand around the iron influences its participation in the Fenton reaction. The ways in which a ligand can influence Fenton reactivity is by limiting access to H_2O_2 as well as modification of the iron redox potential. We propose that the differences observed among the three zeolites is because varying iron coordination on the zeolite surface modifies its participation in the Fenton reaction.

Complexes with smaller reduction potentials such as EDTA (0.12 V) have higher rate constants (10×10^3 L/mol·sec) for the Fenton reaction than complexes with higher reduction potentials such as aqueous complexes of Fe(II), 76 L/mol·sec (0.77 V) (*47,48*). However, Fe-EDTA has a higher rate constant (factor of 10) than Fe-diethylenetriamine pentaacetic acid (DTPA) (E° value of 0.03 V) and has been suggested to arise from unavailable coordination sites in DTPA (*49*). Even for thermodynamically unfavorable reactions, such as with complexes that show a redox potential higher than the reduction potential of the $H_2O_2/OH^-,OH^•$ couple (0.32 V), such as *N,N′*-di-2-picolyl-4,7-diaza-1-oxacyclonanne (DPC), *N,N′,N″*-tri-2-picolyl-1,4,7-triazacyclononane (TPC), or water, with reduction potentials of 0.74, 0.71, and 0.77, respectively, Fenton activity is observed and the involvement of peroxo- complexes in an inner sphere mechanism has been proposed (*50*). This affinity would be higher for DPC than for hexa-aquocomplexes, which would explain the rate constants of 0.65×10^3 and 0.076×10^3 L/mol·sec, respectively, for H_2O and DPC. The differences in rates observed between Fe-DPC and Fe-TPC were attributed to the presence or absence of a free coordination site on the metal; DPC is a pentadentate ligand, TPC is a hexadentate ligand. Singh and Hider (*45*) studied Fe(III) complexes and concluded that a high affinity of a ligand for Fe(III) would stabilize iron in this redox state, hence preventing it from participating further in the Fenton reaction. This is particularly clear in the case of the desferrioxamine ligand (DFO), for which the stability constant with Fe(III) is among the highest (log $K = 30.7$) and for which the rate of substrate hydroxylation via Haber-Weiss mechanism is among the lowest.

Literature regarding the Fenton activity of mineral-bound iron is scarce. Studies have been performed on iron-exchanged mordenite (*51*) and goethite (*52*). Joshi and Limye (*51*) studied the catalytic decomposition of H_2O_2 by Fe(III)-mordenite, but did not conclude if the rate-determining step was the reduction of Fe(III) by the peroxide anion or the reduction of H_2O_2 by Fe(II) (Fenton reaction). Reports of the reduction potential of iron in natural amphibole, magnetite and biotite range from 0.27 to 0.52 V (*53*), values subsequently lower than the reduction potential of iron in water (0.77 V).

The fact that a metal on different zeolites can exhibit different reduction potentials is also suggested by zeolite electrochemistry (*54*). The reduction potential of Cu(II)-exchanged zeolites using cyclic voltammetry show a 30 mV difference in half-wave potential ($E_{1/2}$) between the cyclic voltammograms of copper-exchanged mordenite and copper-exchanged zeolite Y. Because zeolite electrochemistry is a surface phenomenon, these results suggest a difference of the reduction potential for Cu-mordenite and Cu-zeolite Y.

Comparison of the differences in the structure of the zeolites is of interest (*31*). The *a* and *b* axes of erionite represent the fiber surface and shows a network of 8-membered rings (3.6 × 5.1 Å). The natural mordenite sample is not primarily fibrous. Its surface shows channel openings made of 12-membered rings (7.0 × 6.5 Å), 8-membered rings (2.6 × 5.7 Å), and smaller 4-membered rings. Zeolite Y has a more spherical morphology, and its surface presents 12-membered rings (7.4 Å × 7.4 Å). Iron on the zeolite surface is coordinated to the different aluminosilicate rings. The small amounts of hydroxyl radicals produced relative to the surface iron for all samples show that not all iron species on a zeolite surface are Fenton active. This is supported by results from Fubini and co-workers (*55–57*), who have argued that only a few surface iron species on mineral samples are in the right redox and coordination state to be active in the hydroxyl radical generation. This correlates well with the various coordination environments (and their respective abundances) that a zeolite provides for binding iron. The increase in the amounts of radicals per surface iron for erionite is steeper than for mordenite, indicating that erionite surface sites provide a Fenton-enhancing coordination for iron. Zeolite Y shows little or insignificant activity and could arise from binding to the 12-membered rings, which would leave most of the iron coordination sites with water, and therefore its response is comparable to water-coordinated iron in generation of hydroxyl radicals.

Correlation of Biological and Chemical Reactivities

We reached two important conclusions after comparing the results of this study to those in the literature. First, for similar masses of particle exposure, the particle size (presumably by virtue of surface area) has a more significant effect on the oxidative burst upon phagocytosis than the mineral structure. Second, the Fenton chemistry that determines the production of hydroxyl radicals via iron on the zeolites depends on the mineral structure. Thus, while we found that erionite, mordenite, and zeolite Y have comparable oxidative bursts, hydroxyl radical production follows the order erionite > mordenite >> zeolite Y.

Although there is scientific consensus about the adverse effects of erionite in DNA strand breaks (*16*) or mesothelioma induction (*13*), the cytotoxicity of mordenite and zeolite Y has not been extensively studied. Based on aerodynamic diameter calculations, Stephenson et al. (*58*) estimated pulmonary deposition of fiber shaped-mordenite particles

and concluded that substantial deep-lung deposition was possible. Hansen and Mossman (*9*) compared *in vitro* superoxide generation induced by asbestos as well as erionite and mordenite and concluded that mordenite was less active than erionite. They attributed this difference to the fibrous shape of erionite. However, the size distribution of their samples was broad and different for the two zeolites, which casts some uncertainty on the correlation of structure with the oxidative burst. Adamis et al. (*59*) studied *in vitro* and *in vivo* cytotoxicity of well-characterized mordenite samples. *In vivo* studies after intracheal instillation showed acute and subacute inflammation of the lung, which was attributed to the needle-shaped particles (10–12% of the mordenite sample) (*59*). *In vitro* studies showed significant hemolysis but moderate macrophage cell-membrane damage, as compared to quartz. However, the mordenite samples used in these studies could have contained impurities at levels of 45%.

The chemistry of the Fenton reaction at zeolite surface was investigated by Fubini and co-workers (*55–57*). They studied iron-exchanged zeolite Y as well as asbestos and iron oxides and concluded that the extent of hydroxyl radical release did not parallel the mineral iron content or its surface iron content. They used the total iron content and specific surface area, which does not take into account the differences of iron exchange on different coordination sites. In the present study we show, for example, that although mordenite exchanges less total iron than erionite, the surface iron levels are similar. We agree, however, with Fubini et al.'s assessment that only a fraction of the iron species on the mineral surface is in the right redox state and coordination environment to participate in the Fenton reaction (*55–57*).

Thus, the considerable toxicity of erionite may be due to its fibrous nature and size, which ensures penetration into the lungs, and its surface chemistry, which promotes the formation of hydroxyl radicals. Mordenite, with comparable morphology, should also be toxic because of its efficacy in the Fenton reaction, whereas zeolite Y should be considerably less toxic because of its poor Fenton chemistry.

Conclusions

This study focused on two aspects of aluminosilicate mineral chemistry: interactions with macrophage cells (NR8383) and the ability of the mineral surface to produce hydroxyl radicals from H_2O_2 (Fenton reaction). Using ammonium chloride as an endocytosis inhibitor, we have concluded that the dose-dependent chemiluminescence signal due to oxidative burst is mainly from phagocytized particles rather than to particles attached to the membrane. Using size-fractionated samples of the same mineral, we established that the generation of reactive oxygen species is inversely related to the size of the particles for similar levels (by mass) of particle exposure. Iron on the zeolite surface was estimated by exchange with a charged polymer. Hydroxyl radicals generated from H_2O_2 via Fenton reaction and mediated by the Fe(II) zeolites were measured using a chromatographic and a spectrophotometric method. Iron on the surfaces of three different zeolites produced different amounts of hydroxyl radicals and followed the order erionite > mordenite > zeolite Y. We attribute the differences observed between the three zeolites as arising from different coordination of the iron on the zeolite surface. The biological implication of this study is that the size (surface area) of the mineral rather than its structure is the determining factor for the oxidative burst upon phagocytosis, whereas the structure of the mineral plays a key role in determining the production of iron-mediated hydroxyl radicals via the Fenton reaction.

References and Notes

1. Rom WN, Travis WD, Brody AR. Cellular and molecular basis of the asbestos-related diseases. Am Rev Respir Dis 143:408–422 (1991).
2. Crouch E. Pathobiology of pulmonary fibrosis. Am J Physiol 259:L159–L184 (1990).
3. Heppleston AG. Minerals, fibrosis, and the lung. Environ Health Perspect 94:149–168 (1991).
4. De Vuyst P, Dumortier P, Swaen GMH, Pairon JC, Brochard P. Respiratory health effects of man-made vitreous (mineral) fibers. Eur Respir J 8:2149–2173 (1995).
5. Dörger M, Münzing S, Allmeling A-M, Messmer K, Krombach F. Differrential responses of rat alveolar and peritoneal macrophages to man-made vitreous fibers *in vitro*. Environ Health Res A 85:207–214 (2001).
6. Quinlan TR, BeruBe KA, Marsh JP, Janssen YMW, Taishi P, Leslie KO, Hemenway D, O'Shaughnessy PT, Vacek P, Mossman BT. Patterns of inflammation, cell proliferation, and related gene expression in lung after inhalation of chrysotile asbestos. Am Pathol 147:728–739 (1995).
7. Maples KR, Johnson NF. Fiber-induced hydroxyl radical formation: correlation with mesothelioma induction in rats and humans. Carcinogenesis 13:2035–2039 (1992).
8. Kane AB, Boffetta P, Saracci R, Wilbourn JD, eds. Mechanisms of Fiber Carcinogenesis. IARC Sci Publ 140, 1996.
9. Hansen K, Mossman BT. Generation of superoxide (O_2^-) from alveolar macrophages exposed to asbestiform and nonfibrous particles. Cancer Res 47:1681–1686 (1987).
10. Xu A, Wu LJ, Santella RM, Hei TK. Role of oxyradicals in mutagenicity and DNA damage induced by crocidolite asbestos in mammalian cells. Cancer Res 59:5922–5926 (1999).
11. Janero DR. Malondialdehyde and thiobarbituric acid-reactivity as diagnostic indices of lipid peroxidation and peroxidative tissue injury. Free Radical Biol Med 9:515–540 (1990).
12. Refsgaard HHF, Tsai L, Stadtman ER. Modifications of proteins by polyunsaturated fatty acid peroxidation products. Proc Natl Acad Sci USA 97:611–616 (2000).
13. Wagner JC, Skidmore JW, Hill RJ, Griffiths DM. Erionite exposure and mesotheliomas in rats. Br J Cancer 51:727–730 (1985).
14. Mossman BT, Sesko AM. In vitro assays to predict the pathogenicity of mineral fibers. Toxicology 60:53–61 (1990).
15. Timblin CR, Guthrie GD, Janssen YWM, Walsh ES, Vacek P, Mossman BT. Patterns of c-*fos* and c-*jun* proto-onocogene expression, apoptosis, and proliferation in rat pleural mesothelial cells exposed to erionite or asbestos fibers. Toxicol Appl Pharamacol 151:88–97 (1998).
16. Eborn SK, Aust A. Effect of iron acquisition on induction of DNA single-strand breaks by erionite, a carcinogenic mineral fiber. Arch Biochem Biophys 316:507–514 (1995).
17. Guthrie GD. Biological effects of inhaled minerals. Am Mineral 77:225–243 (1992).
18. Palekar LD, Most BM, Coffin DL. Significance of mass and number of fibers in the correlation of V79 cytotoxicity with tumorigenic potential of mineral fibers. Environ Res 46:142–152 (1988).
19. Helmke RJ, Boyd RL, German VF, Mangos JA. From growth factor dependence to growth factor responsiveness: the genesis of an alveolar macrophage cell line. In Vitro Cell Dev Biol 23:567–574 (1987).
20. Hogg BD, Dutta PK, Long JF. In vitro interaction of zeolite fibers with individual cells (macrophages NR8383): measurement of intracellular oxidative burst. Anal Chem 68:2309–2312 (1996).
21. Long JF, Dutta PK, Hogg BD. Fluorescence imaging of reactive oxygen metabolites generated in single macrophage cells (NR8383) upon phagocytosis of natural zeolite (erionite) fibers. Environ Health Perspect 105:706–711 (1997).
22. Fritz JS, Schenk GH. Chapter 13. In: Quantitative Analytical Chemistry. Boston:Allyn and Bacon, Inc., 1969;265–284.
23. Daniels RH, Kerr GT, Rollman LD. Cationic polymers as templates in zeolite crystallization. J Am Chem Soc 100:3097–3100 (1978).
24. Babbs C, Steiner MG. Detection and quantitation of hydroxyl radical using dimethyl sulfoxide as molecular probe. Meth Enzymol 186:137–147 (1990).
25. Steiner MG, Babbs CF. Quantitation of the hydroxyl radical by reaction with dimethyl sulfoxide. Arch Biochem Biophys 278:478–481 (1990).
26. von Ballmoos R, Higgins JB. Collection of simulated x-ray powder patterns for zeolites. Zeolites 10:313–520 (1990).
27. Flanigen EM. Use of natural zeolites in agriculture and aquaculture. In: Zeo Agriculture (Pond WG, Mumpton FA, eds). Boulder, CO:Westview Press, 1984;55–68.
28. Wright WE, Rom WN, Moatamed F. Characterization of zeolite fiber sizes using scanning electron microscopy. Arch Environ Health 38:99–103 (1983).
29. Stringer B, Kobzik L. Measurement of environmental particulate uptake by lung cells using flow cytometry. Methods Mol Biol 91:109–116 (1998).
30. Ng KY, Stringer KA, Cohen Z, Serravo R, Tian B, Meyer JD, Falk R, Randolph T, Manning MC, Thompson DC. Alveolar macrophage cell line is not activated by exposure to polymeric microspheres. Int J Pharm 170:41–49 (1998).
31. Breck, DW. Zeolite Molecular Sieves. New York:Wiley, 1974.
32. Bordiga S, Buzzoni R, Geobaldo F, Lamberti C, Giamello E, Zecchina A, Leofanti G, Petrini G, Tozzola G, Vlaic G. Structure and reactivity of framework and extraframework iron in Fe-silicalite as investigated by spectroscopic and physicochemical methods. J Catal 158:486–501 (1996).
33. Tuel A, Arcon I, Millet JM. Investigation of structural iron species in Fe-mesoporous silicas by spectroscopic techniques. J Chem Soc Faraday Trans 94:3501–3510 (1998).
34. Bordiga S, Buzzoni R, Geobaldo F, Lamberti C, Giamello E, Zecchina A, Leofanti G, Petrini G, Tozzola G, Vlaic G. Structure and reactivity of framework and extraframework iron in Fe-silicalite as investigated by spectroscopic and physicochemical methods. J Catal 158:486–501 (1996).
35. Pearce JR, Mortier WJ, Uytterhoeven JB, Lunsford JH. Crystallographic study of the distribution of cations in Y-type zeolites containing iron(2+) and iron(3+). J Chem Soc Faraday Trans 1:937–946 (1981).
36. Royall JA, Ischiropoulos H. Evaluation of 2′,7′-dichlorofluorescin and dihydrorhodamine 123 as fluorescent probes for intracellular hydrogen peroxide in cultured endothelial cells. Arch Biochem Biophys 302:348–355 (1993).
37. Hempel SL, Buettner GR, O'Malley YQ, Wessels DA, Flaherty DM. Dihydrofluorescein diacetate is superior for detecting intracellular oxidants: comparison with 2′,7′-dichlorodihydrofluorescein diacetate, 5(and 6)-carboxy-2′,7′-dichlorodihydrofluorescein diacetate, and dihydrorhodamine 123. Free Rad Biol Med 27:146–159 (1999).
38. Ci YX, Tie JK, Yao JF, Liu ZL, Lin S, Zheng W. Catalytic behavior of iron(II)-oxime complexes in the chemiluminescence reaction of luminol with hydrogen peroxide. Anal Chim Acta 277:67–72 (1993).
39. Bass DA, Parce JW, DeChatelet LR, Szejda P, Seeds MC, Thomas M. Flow cytometric studies of oxidative product formation by neutrophils: a graded response to membrane stimulation. J Immunol 130:1910–1917 (1983).

40. Nadeau D, Vincent R, Kumarathasan P, Brook J, Dufresne A. Cytotoxicity of ambient air particles to rat lung macrophages: comparison of cellular and functional assays. Toxicol In Vitro 10:161–172 (1996).
41. Urano N, Yano E, Evans PH. Reactive oxygen metabolites produced by the carcinogenic fibrous mineral erionite. Environ Res 54:74–81 (1991).
42. Helmke RJ, German VF, Mangos JA. A continuous alveolar macrophage cell line: comparisons with freshly derived alveolar macrophages. In Vitro Cell Dev Biol 25:44–48 (1989).
43. Richeson CE, Mulder P, Bowry VW, Ingold KU. The complex chemistry of peroxynitrite decomposition: new insights. J Am Chem Soc 120:7211–7219 (1998).
44. Meier WM, Olson DH. Atlas of Zeolite Structure Types. Stoenham, MA:Butterworth-Heinemann, 1992.
45. Singh S, Hider RC. Colorimetric detection of the hydroxyl radical: comparison of the hydroxyl-radical-generating ability of various iron complexes. Anal Biochem 171:47–54 (1998).
46. Ulanski P, Merenyi G, Lind J, Wagner R, von Sonntag C. The reaction of methyl radicals with hydrogen peroxide. J Chem Soc Perkins Trans 2:673–676 (1999).
47. Addy RA, Gilbert BC. Iron-ligand interaction and the Fenton reaction. In: Handbook of Metal-Ligand Interactions in Biological Fluids. Vol. 2. Bioinorganic Chemistry (Berthon G, ed). New York:Marcel Dekker, Inc., 1995;857–866.
48. Walling C. Fenton's reagent revisited. Acc Chem Res 8:125–131 (1975).
49. Graf E, Mahoney JR, Bryant RG, Eaton JW. Iron-catalyzed hydroxyl radical formation. Stringent requirement for free iron coordination site. J Biol Chem 259:3620–3624 (1984).
50. Szulbinski WS. Fenton reaction of iron chelates involving polyazacyclononane. The ligand structure effect. Pol J Chem 74:109–124 (2000).
51. Joshi R, Limye SN. Catalytic activities of transition metal complexes on zeolites for the decomposition of H_2O_2. Oxidat Commun 21:337–341 (1998).
52. Chen PH, Watts RJ. Determination of rates of hydroxyl radical generation in mineral-catalyzed Fenton-like oxidation. J Chin Inst Environ Eng 10:201–208 (2000).
53. White AF, Peterson ML, Hochella MF Jr. Electrochemistry and dissolution kinetics of magnetite and ilmenite. Geochim Cosmochim Acta 58:1859–1875 (1994).
54. Senaratne C, Zhang J, Baker M, Bessel CA, Rolison DR. Zeolite-modified electrodes: intra- versus extra-zeolite electron transfer. J Phys Chem 100:5849–5862 (1996).
55. Fubini B, Mollo L, Giamello E. Free radical generation at the solid/liquid interface in iron containing minerals. Free Rad Res 23:593–614 (1995).
56. Prandi L, Bodoardo S, Penazzi N, Fubini B. Redox state and mobility of iron at the asbestos surface: a voltammetric approach. J Mater Chem 11:1495–1501 (2001).
57. Fubini B, Mollo L. Role of iron in the reactivity of mineral fibers. Toxicol Lett 82/83:951–960 (1995).
58. Stephenson DJ, Fairchild CI, Buchan RM, Dakins ME. A fiber characterization of the natural zeolite, mordenite: a potential inhalation health hazard. Aerosol Sci Technol 30:467–476 (1999).
59. Adamis Z, Tatrai E, Honmas K, Six E, Ungvary G. In vitro and in vivo tests for determination of the pathogenicity of quartz, diatomaceous earth, mordenite, and clinoptilolite. Ann Occup Hyg 44:67–74 (2000).